SAE INTERNATIONAL

ARTICLE INFO

Article ID: 03-17-08-0060

doi:10.4271/03-17-08-0060

Numerical Investigation of Premixed and Non-premixed Ammonia Main Charge Configurations Ignited by a Hydrogen-Fired Prechamber

Thomas Indlekofer,[1] Nils Erland Haugen,[1] Olav Øyvind Førde,[2] and Andrea Gruber[1]

[1]SINTEF Energy Research, Norway
[2]Norwegian University of Science and Technology, Department of Energy and Process Engineering, Norway

Abstract

Ammonia-fired reciprocating engines have emerged as a promising technology in the maritime and power generation sector at medium-to-large scale (1–80 MW). The use of "on-the-fly" partial ammonia decomposition to produce a relatively small amount of hydrogen that can be used as combustion promoter, replacing fossil fuels in this function, enables this technology to provide carbon-free propulsion and power generation. In this context, it is envisioned that a hydrogen-fired prechamber ignition strategy offers significant advantages by accelerating the ammonia ignition and complete combustion process, increasing its reliability and robustness while still aiming to achieve low NO_x, N_2O, and NH_3 emissions. This study exploits an OpenFOAM-based Large Eddy Simulation (LES) numerical modeling framework to investigate the ignition and combustion behavior of an ammonia main charge ignited by a hydrogen-fired prechamber. First, a conventional port-injection premixed configuration for the ammonia main charge is considered whereas the hydrogen-fired prechamber is found to provide a sufficiently strong ignition source for all ammonia–air mixtures investigated. The effect of the main charge equivalence ratio and the wall temperature on combustion efficiency and emissions formation is evaluated. Second, considering a non-premixed configuration for comparison, an identically configured hydrogen-fired prechamber is used to study the ignition and combustion process for ammonia main charges directly injected as liquid sprays and modeled as Lagrangian particle tracking (LPT) in conjunction with the LES model. The LES results suggest that the relative timing and angle of injection between the liquid sprays and the hydrogen jet flames emerging from the prechamber play a major role in controlling the ignition and combustion process. Finally, the non-premixed ammonia main charge configuration is found to significantly reduce the formation of pollutants and extend the operating range to leaner global equivalence ratios, compared to the premixed ammonia main charge configuration.

History

Received: 29 Dec 2023
Revised: 09 May 2024
Accepted: 26 Jul 2024
e-Available: 14 Aug 2024

Keywords

Ammonia, Hydrogen, Internal combustion engine, Prechamber ignition, Turbulent jet ignition, Large eddy simulation, Combustion

Citation

Indlekofer, T., Haugen, N., Førde, O., and Gruber, A., "Numerical Investigation of Premixed and Non-premixed Ammonia Main Charge Configurations Ignited by a Hydrogen-Fired Prechamber," *SAE Int. J. Engines* 17(8):2024, doi:10.4271/03-17-08-0060.

ISSN: 1946-3936
e-ISSN: 1946-3944

This article is part of a focus issue on Fossil-Free Alternate Fuel Technology for IC Engines.

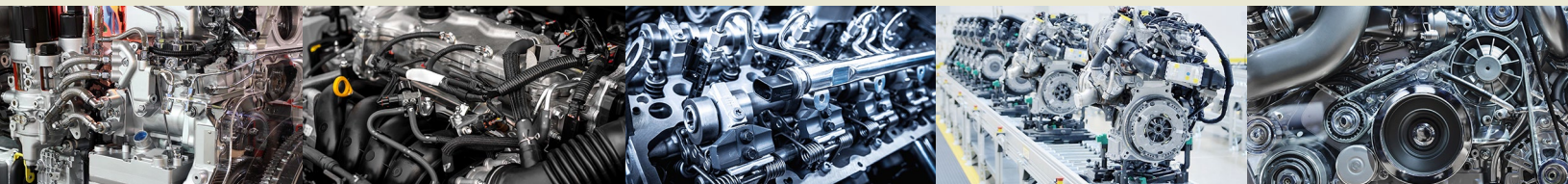

1. Introduction

Hydrogen and ammonia have been identified as viable energy vectors to decarbonize the maritime and power generation sectors. Hydrogen, specifically, has been referred to as a facilitator of a carbon-neutral economy. However, challenges associated with hydrogen storage, transport, distribution, and infrastructure deployment have impeded, to date, its integration into the energy system. Conversely, ammonia emerges as an efficient carbon-free hydrogen carrier, characterized by a high energy density and a well-established, adaptable infrastructure capable of addressing several of the primary limitations of hydrogen. Recently, the use of ammonia in internal combustion engines is being considered within the maritime sector [1] that alone is responsible for 3–4% of GHG emissions in the EU [2], with similar figures applicable globally.

The use of ammonia in internal combustion engines is not novel. In 1935, the first "hydrogen car" traveled for more than 600 km from Terni to Trieste. It was a FIAT 509 with an ammonia-powered engine designed and built by Casale [3]. Based on Casale's initial patents the Gazamo process was developed and tested on the road in 1941, which appears to be the first large-scale application of ammonia as a fuel in vehicles [4]. While those early experiences and subsequent work by the United States Army in the 1960s [5] generally indicated the potential of ammonia as a fuel, it never materialized in the commercialization of ammonia-powered engines. However, in the pursuit of sustainable and low-carbon energy solutions, there has been a notable resurgence in the exploration of ammonia as a viable alternative fuel for diverse engine applications [6]. This renewed interest is driven by the urgent need to mitigate environmental impact and reduce carbon emissions associated with conventional fuels.

In terms of its combustion properties, ammonia faces several challenges compared to the predominant hydrocarbon fuels. It has a high ignition temperature, low flame speed, narrow flammability window, high heat of vaporization, slow chemical kinetics, and, due to the fuel-bound nitrogen, combustion of ammonia is prone to formation of NO_x or N_2O [7]. While NO_x represents harmful, and strictly regulated, atmospheric pollutants, N_2O is globally the third most important greenhouse gas after methane and carbon dioxide, as it has 300 times the warming potential of carbon dioxide. The inferior combustion properties of ammonia mean that different combustion strategies than those of hydrocarbon fuels are needed [8]. In practice, this means that one has to overcome the low reactivity of ammonia while limiting the pollutant formation. Early research in the 1960s indicated successful combustion of pure ammonia in compression ignition (CI) engines only for extremely high compression ratios larger than 35:1 and under very specific engine conditions [5]. Subsequently, recent research in CI engines has focused on dual-fuel strategies, where a more reactive secondary fuel is used either as an ignition source or admixed to increase the reactivity of the mixture. Often, these solutions depend on fossil fuels, such as diesel [9, 10], which produce carbon emissions.

As an alternative, hydrogen, which is highly reactive and has a low ignition energy and high flame speed, can be used as a carbon-free combustion promoter for ammonia [11]. This brings another advantage, allowing to circumvent an extra storage system for a second fuel, as hydrogen can be produced by in situ NH_3 decomposition [12]. Based on experiments in a spark-ignited (SI) engine, Mørch et al. [13] reported that the efficiency and mean effective pressure were highest at mixtures containing at least 10 vol.% hydrogen in the fuel. Similar trends were observed by Frigo et al. [14], reporting that 7 vol.% H_2 at full load and 11 vol.% at half load are needed to ensure stable engine operation, but with reduced performance with respect to gasoline operation. However, this strategy led to significant NO_x emissions, necessitating aftertreatment [13], and best performance was observed for stoichiometric conditions, which leads to ammonia slip. Accordingly, it is evident that simply admixing a more reactive fuel to ensure satisfactory combustion properties does not completely solve the challenges of ammonia as a fuel in internal combustion engines.

Previously used to enable operation of lean premixed combustion of fossil fuels, prechamber ignition is a technology that is relevant for ammonia-fired engines, which face similar issues due to low reactivity [15]. This strategy makes use of a prechamber of only a fraction of the size of the main chamber, in which combustion leads to a pressure increase pushing premixed gas followed by hot combustion products through several ducts into the main chamber, creating strong turbulence and serving as high energy ignition sources [16]. Prechambers are known to increase the flammability limit, reduce cycle-to-cycle variations, reduce the risk of misfiring, and lead to a shorter flame travel time toward the piston top-land crevice, thereby possibly reducing unburnt fuel emissions [15]. To eliminate CO_2 emissions, hydrogen as a prechamber fuel has been proposed [17]. Several recent studies have reported that hydrogen prechambers accelerate the ammonia combustion process and improve the combustion stability significantly [18, 19, 20]. A recent review by Zhou et al. [21] introduces two prechamber strategies for ignition of the main charge: a "Mode 2" configuration consisting of prechamber originated turbulent jet flames issuing into port-injected ammonia premixed with air and a "Mode 3" where the prechamber jet flames interact with liquid sprays of directly injected ammonia. While numerical and experimental investigations have been conducted on the "Mode 2" configuration [18, 19, 20], "Mode 3" has to date only been discussed conceptually.

In the present work, we aim to close this gap and consider the latter non-premixed configuration, which is particularly interesting with respect to the minimization of unburnt fuel and emissions, comparing its performance to the premixed configuration. Non-premixed combustion, a characteristic feature of direct-injected liquid fuels, leads to locally quasi-stoichiometric and fuel-rich reaction layers throughout the turbulent flame brush and is linked to lower formation of undesired pollutants (NO_x) from ammonia oxidation [22, 23, 24]. Furthermore, very recent findings have related N_2O accumulation in the products of premixed ammonia combustion

to flame quenching on (relatively) cold surfaces [25]. This situation, flame quenching on the cylinder walls and crevices, typically affects port-injected, premixed configurations to a significantly larger extent compared to direct-injection, non-premixed configurations. The present manuscript is structured as follows: in Section 2 the configurations considered in this work are presented while Section 3 describes the numerical model and the simplifying assumptions adopted. Section 4 illustrates the results from the numerical simulations, providing a validation of the ammonia spray injection in Section 4.1 and comparing the premixed and the non-premixed combustion configurations in Sections 4.2 and 4.3, respectively. Section 5 summarizes the present findings, presenting some conclusions that can be exploited in the design of clean and efficient ammonia-fired internal combustion engines.

2. Case Configuration

This work investigates two alternative combustion configurations of relevance to internal combustion engines, see the sketch presented in Figure 1. In a recent review by Zhou et al. [21] these two configurations are denoted as "Mode 2" and "Mode 3" for reactivity-controlled turbulent jet flame ignition of an ammonia-fired engine. Both "Modes" make use of a prechamber to ignite the main charge.

In the present investigation, the prechamber is filled with a mixture of fully decomposed ammonia and air ($H_2/N_2/O_2$) at stoichiometric conditions (equivalence ratio $\phi = 1$) and contains approximately 1% of the total chemical energy of the fuel, i.e., the remaining 99% is in the main charge, see Table 1. The rationale behind using a mixture of decomposed ammonia and air is that this corresponds to a scenario that circumvents a secondary tank for the prechamber fuel (hydrogen), but makes use of a cracker, which is a part of the main fuel (ammonia) that is diverted to provide decomposed ammonia. The high reactivity of hydrogen ensures a rapid consumption of the prechamber fuel, leading to thermal expansion and a pressure increase that pushes the hot reacted gases into the main chamber, while generating strong turbulence induced by the shear between the hot jet flame and the surrounding mixture of ammonia and air, thereby facilitating robust ignition of the less reactive ammonia main charge. All simulations are initiated with a chamber pressure $p = 40$ bar. In a realistic engine scenario the flow field is typically highly turbulent with tumbling or swirling flow, which affects the mixing and combustion. However, for the current study, all cases are initialized with identical quiescent-flow conditions, which provides valuable insight about the comparative behavior of the different configurations.

FIGURE 1 A qualitative sketch of the two configurations investigated: (a) hydrogen-fired prechamber igniting premixed NH_3–air, (b) side view, and (c) top view of hydrogen-fired prechamber igniting liquid NH_3 sprays.

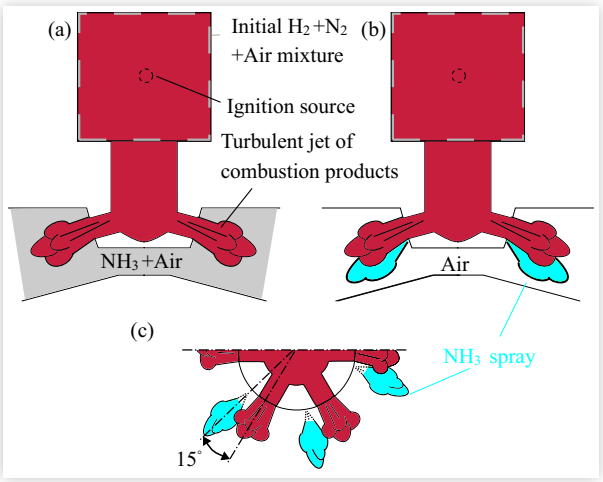

For the premixed combustion configuration, the main charge is represented by a homogeneous mixture of ammonia and air. This homogeneous mixture corresponds to an idealization of the case where either liquid or gaseous ammonia is injected into the intake manifold and enters the main chamber after mixing with air. Simulations have been performed for a range of global equivalence ratios present in the main chamber in Cases 1–4 (ϕ = 0.6, 0.8, 1.0, 1.2). This covers a range from very lean to stoichiometric, where a significant production of NO and N_2O is expected, to rich conditions, where ammonia flames are reported to produce less NO and N_2O [26]. The initial gas temperature for the premixed combustion configuration is 860 K, based on the isentropic combustion of air to 40 bar. Most calculations are performed for wall temperatures of T_w = 700 K. However, the effect of different wall temperatures, T_w = 500, 600 K, is investigated for the premixed cases with $\phi = 1$ in Cases 5–7.

For the non-premixed combustion configuration, the ammonia main charge is injected as liquid sprays over a period of 1 ms, with the mass of liquid ammonia adapted to achieve a global equivalence ratio equivalent to those considered in the stoichiometric premixed configuration (Cases 8–12). The initial gas temperature for the non-premixed cases is 980 K. The reason for the higher initial temperature compared to the premixed cases is that it results in a final temperature of 860 K for the mixture of fully evaporated ammonia and air. Cases 8–12 introduce a variation of an additional control parameter for the non-premixed combustion configuration that is crucially important: the ignition timing of the prechamber relative to the initiation of the liquid ammonia injection, denoted as t_{ign}. More specifically, t_{ign} is defined as the time it takes from the start of spray injection until the prechamber is ignited by the spark. This timing strongly affects the ignition and combustion behavior of the sprays within the main chamber as discussed in Section 4.3. Finally, Case 13 considers a global fuel-lean main charge in the non-premixed combustion configuration for comparison with the homogeneous premixed combustion configuration (Case 1). The main parameters characterizing the premixed and non-premixed configurations investigated are summarized in Table 1.

TABLE 1 Main parameters for Cases 1–13 representing the premixed and non-premixed combustion configurations: the prechamber energy fraction based on the lower heating value, the global equivalence ratio in the main chamber ϕ_{main}, the gas and wall temperature T_g/T_w, and the ignition timing of the spray cases t_{ign}.

	Mode	E_{pre}/E_{tot} [%]	ϕ_{main}	T_g [K]	T_w [K]	t_{ign} [ms]
1	Pre	1.38	0.6	860	700	0
2	Pre	1.08	0.8	860	700	0
3	Pre	0.91	1.0	860	700	0
4	Pre	0.79	1.2	860	700	0
5	Pre	0.91	1.0	860	500	0
6	Pre	0.91	1.0	860	550	0
7	Pre	0.91	1.0	860	600	0
8	Spray	0.82	1.0	980	700	0
9	Spray	0.82	1.0	980	700	0.3
10	Spray	0.82	1.0	980	700	0.5
11	Spray	0.82	1.0	980	700	0.7
12	Spray	0.82	1.0	980	700	1.0
13	Spray	1.36	0.6	980	700	0.5

A 2D representation of the full 3D geometry of the computational domain is shown in Figure 2, and it is meant to represent a generic marine diesel engine design. The prechamber is represented as a cylinder, which through a narrower throat and six nozzles connects it to the main chamber. The piston bowl geometry is ω-shaped, and it is similar to the one presented by Pham et al. [27]. It is important to note that in the present investigation, the motion of the piston is neglected since the focus is devoted to high-resolution simulations representing the prechamber ignition process, the formation and issuing of the turbulent hydrogen jet flames into the main combustion chamber, the ammonia spray evaporation and ignition processes, and the combustion process and emissions formation within the combustion chamber. The injection of the ammonia droplets is assumed to happen through six sprays of liquid ammonia entering the combustion chamber via injection nozzles located at a radial distance of r_{spray} = 12 mm from its center and separated by a 15° angle from the prechamber jet flames inlet direction, as shown in Figure 1. The 15° angle between the spray and prechamber nozzle was chosen to ensure a strong interaction, facilitating ignition. Some additional geometric parameters are described in Table 2.

FIGURE 2 Left-hand side of the pre- and main combustion chamber geometry with major dimensions in mm.

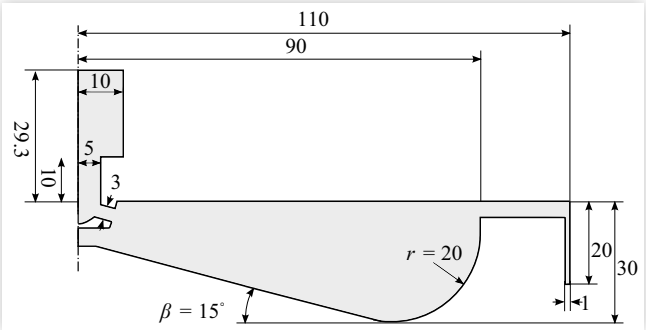

Before concluding the present section it is important to note that, within the scope of the present modeling investigation consisting of high-resolution numerical simulations, we assume that any eventual issue with the practical implementation of concurrently placed prechamber and liquid fuel injector within the cylinder head can be solved with novel and improved designs.

3. Numerical Model Formulation

In this section, a concise overview is provided for the primary characteristics of the numerical and physical models employed in the present work. The C++ library OpenFOAM [28], an open-source collection, serves as a platform for discretizing partial differential equations through finite-volume methods. The simulation of reactive flows involves the utilization of a compressible, multicomponent, and multi-phase solver (sprayFOAM), coupled with a large eddy simulation (LES) turbulence model and a partially stirred reactor (PaSR) model for turbulence–chemistry interactions.

TABLE 2 Main geometric parameters.

Volume prechamber V_{pre}	6.06×10^{-6} m^3
Volume nozzle region V_{noz}	1.48×10^{-6} m^3
Volume main chamber V_{main}	6.15×10^{-4} m^3
$(V_{pre} + V_{noz})/V_{tot}$	1.2%
Number of prechamber nozzles	6
Number of ammonia spray nozzles	6

The governing equations solved are the Navier–Stokes equations for mass and momentum, as well as the conservation equations for energy and species. The representation of the liquid phase is based on a Lagrangian particle tracking (LPT) approach in which liquid droplets are assumed spherical and of constant size, thereby circumventing the significant challenges related to detailed modeling of the primary break up of the spray. Consequently, the input parameters that are required to characterize the ammonia sprays are validated in Section 4.1 against available experimental data. To facilitate pressure–velocity coupling, the PIMPLE algorithm, a hybrid SIMPLE-PISO iteration scheme, is employed, enabling the use of larger time steps. An adaptive time step is employed, constrained by a user-defined Courant number (<0.5). Time integration relies on an implicit first-order Euler scheme, with the actual time step decreasing to a value around 10 ns for the time period characterized by the highest velocities within the prechamber nozzles. Face flux interpolation to cell values is achieved through combinations of second-order central differencing schemes.

The one-equation eddy viscosity model, which solves a transport equation for subgrid-scale turbulent kinetic energy is used in conjunction with the LES framework. The chemical kinetics scheme selected to represent the combustion process is a recently updated short version of the San Diego mechanism, featuring 19 species and 63 elementary steps, that include both the hydrogen and nitrogen subsets [29].

The computational mesh is created with the OpenFOAM tool snappyHexMesh. A uniform cell size x_{cell} = 500 µm over the whole geometry is chosen with predominantly hexahedral cells. The total cell count is 9.6 million cells.

3.1. Simulation Procedure

For both the premixed and non-premixed combustion configurations, the prechamber volume is filled with a homogeneous mixture of fully decomposed ammonia and air at stoichiometric equivalence ratio. Prechamber ignition is achieved by imposing a spherical volume with r_{ign} = 1 mm to a burnt state in the center of the prechamber volume. The corresponding mass fractions and temperature values are extracted from a Cantera simulation of an adiabatic freely propagating flame. In the premixed combustion configuration this ignition is assumed to take place at t = 0 for all cases investigated, while the prechamber ignition timing relative to the initiation of the liquid ammonia spray injection is varied in the non-premixed combustion configuration. All cases are simulated until t = 20 ms.

4. LES Results

4.1. Ammonia Spray Validation

While diesel and gasoline sprays have been extensively investigated during the last few decades, and practices for LES have been developed, research on ammonia sprays is still scarce. This section aims to validate the chosen LES approach for the prediction of ammonia sprays by comparison with two experimental data sets. The first data set is provided by Scharl et al. and corresponds to a subset of the data presented in their recent works [10, 30]. Experiments are performed in a rapid compression–expansion machine with ammonia injections performed into an oxygen-depleted environment ensuring non-reactive conditions. While the validation is performed for several chamber pressures, the discussion will be limited to the case with p = 75 bar for brevity. The nozzle diameter is d_{nozzle} = 0.94 mm. The second data set corresponds to data from a constant volume combustion chamber presented by Li et al. [31]. This data corresponds to a quite different condition with a lower chamber pressure of p = 16 bar and d_{nozzle} = 0.22 mm. After setting the relevant injection parameters (pressure, temperature, nozzle size, injection profile) based on the experiments, an initial particle size distribution and spray angle have to be assumed. As the chosen LES approach circumvents modeling of the primary spray break up to reduce the complexity of the simulations, the initial particle size is tuned to a value that captures the liquid penetration depth from the experiments following a well-established methodology developed for diesel sprays [32]. In the present work, a droplet size of $d_{droplet}$ = 3 µm is found to give the best results. The spray angle was estimated based on the experimental results and on a literature review by Haugsvar [33] to a half cone angle of γ = 24°. Figure 3(a) compares the vapor penetration depth for the Scharl experiment with the simulation results. As evidenced by the plot, a good prediction of the vapor penetration depth and the general spray shape (inlet) is achieved. Figure 3(b) displays the liquid and vapor penetration depth for the Li experiment and for the LES prediction. Both are slightly underpredicted at the initial stages of the injection but, as soon as the final liquid penetration depth is

FIGURE 3 Validation of the modeling approach for ammonia spray injection. (a) Vapor penetration depth and overall spray shape compared to experiments and (b) liquid and vapor penetration depth compared to experiments.

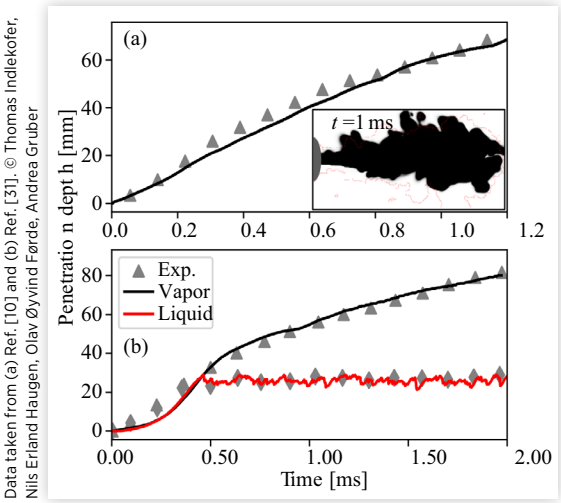

Data taken from (a) Ref. [10] and (b) Ref. [31]. © Thomas Indlekofer, Nils Erland Haugen, Olav Øyvind Førde, Andrea Gruber

reached, both liquid and vapor penetration compare well with the experiments. The overall quality of the LES prediction for the ammonia sprays is satisfactory. For the non-premixed combustion configuration investigated in this work, a similar nozzle to the one in the Li experiments is assumed and the spray parameters identified in the validation are used.

4.2. Premixed NH_3–Air Combustion

Effect of the Equivalence Ratio This section presents the numerical predictions from the prechamber-ignited premixed configurations for different equivalence ratios. Figure 4 displays the instantaneous temperature contour plots for increasing time. At t = 0.1 ms the turbulent jet from the prechamber enters the main chamber. In Cases 2–4 (ϕ = 0.8 – 1.2) the hot gases ignite the main ammonia charge in the jet flame shear layer. In Case 2, the flame is more broken-up and fragmented and propagates at a slower rate. In Case 4 the flame initially expands faster than in Case 3 (between t = 0.1 – 0.3 ms) but, after this time, the development of both flames is very similar except for the higher flame temperature in the stoichiometric mixture. Conversely, the jet fails to immediately ignite the main charge in Case 1 and, as revealed by the time history of the integrated total fuel mass shown in Figure 5, ignition occurs much later, at a time $t \sim 2$ ms, and progresses very slowly due to the low burning rate of the leaner ammonia flame, needing almost 16 ms to achieve complete combustion. It is evident that the burning rate at this low equivalence ratio is much too slow to be practically implemented in internal combustion engines. Figure 5 also clearly illustrates the rapid ammonia consumption at the initial ignition stage in Case 3 compared to the other ones. The ammonia surplus in the fuel-rich case is mostly decomposed to hydrogen by the high flame temperature at adiabatic conditions, remaining as unburnt fuel in the combustion chamber. Also, notable is the fact that a minimal amount of unburnt ammonia remains in the combustion chamber due to flame quenching taking place in the crevices independently of the equivalence ratio considered. This process is shown in Figure 6, exemplary for Case 3. Overall, the consumption of NH_3 occurs at the flame front, as can be seen by comparison with Figure 4. However, at later stages, the flame is quenched in the crevice and the resulting unburnt NH_3 leaks back into the chamber. In terms of the pollutant formation, Figure 5 shows the time history of the integrated total mass of NO_x (sum of NO and NO_2) and N_2O normalized by the overall lower heating value of the hydrogen and ammonia fuel. For all cases, NO_x and N_2O peaks are observed in correspondence with the initial ignition and consumption of the ammonia fuel. However, a relatively large fraction of these undesired species that are initially formed is then consumed as the combustion process evolves in time. In terms of NO, it is well-established that ammonia oxidation

FIGURE 4 Temperature contours for Cases 1–4. Rows correspond to ϕ = 0.6–1.2 and columns to different time instants.

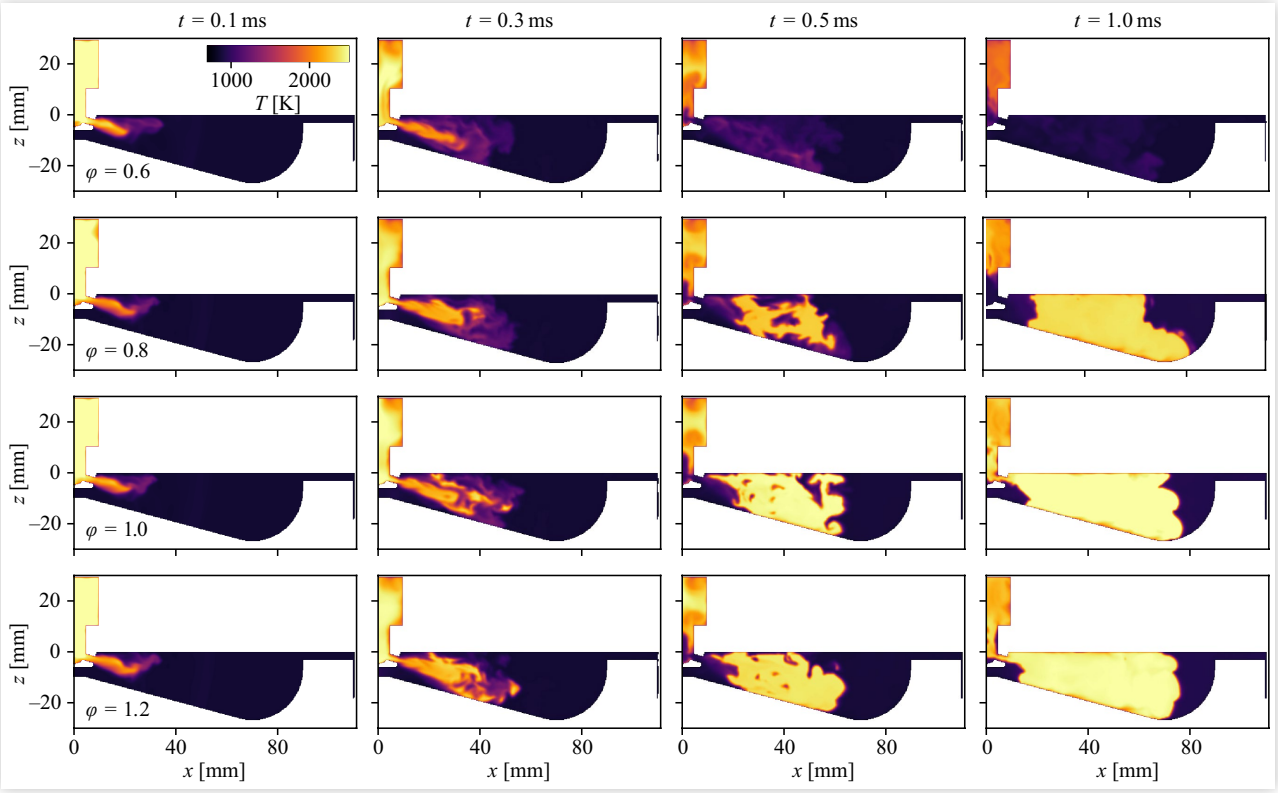

FIGURE 5 Time history of the integrated total mass of species NH_3, H_2 (a, b), and energy input-normalized NO_x and N_2O (c, d) for Cases 1–4.

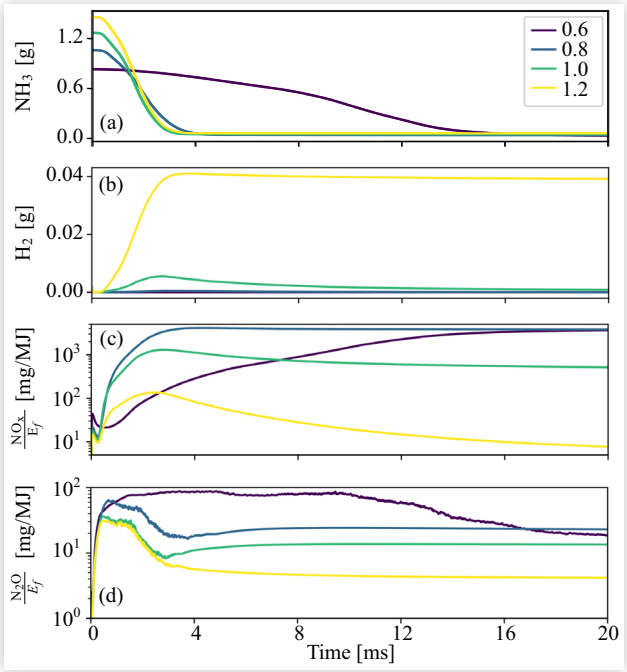

exhibits a peak in NO formation around $\phi = 0.8–0.9$ [22] with significantly reduced values for rich conditions, as also evidenced by the present predictions. At lean conditions, for Cases 1 and 2, NO_x emissions of 4000 mg MJ^{-1} are observed. The stoichiometric Case 3 exhibits NO_x emissions of 550 mg MJ^{-1} while these emissions are further reduced (to ≈ 10 mg MJ^{-1}) in the fuel-rich case. Figure 7 shows that the ignition process in the prechamber leads to locally high values of NO, followed by further formation of NO in the ammonia flame. While NO values are reduced at later time instants for rich conditions, this reduction is not observed at the same magnitude (relatively) for the lean conditions. Based on unstretched 1D flame simulations the production of N_2O is reported to increase significantly for rich conditions [22]. However, the abundance of unburnt molecular hydrogen, and of H radicals in the hot regions close to the flame reaction layer, promotes the consumption of N_2O through the $N_2O + H = N_2 + OH$ reaction [34]. Accordingly, the lowest N_2O emissions are observed in Case 4 at fuel-rich conditions. The formation of N_2O is further investigated in Figure 8, which shows that N_2O formation is clearly linked to the flame front of the ammonia flame (no N_2O formation during hydrogen combustion in the prechamber). A significant amount of N_2O then gets consumed in the environment of hot combustion products, while this process is hindered in cold conditions that specifically occur in the crevice region, where the cold walls have a strong cooling effect on the gases. While the absolute values differ depending on ϕ, the remaining N_2O can be linked to the crevice region for all cases.

Effect of the Wall Temperature A recent work by Zhou et al. [35] describes the possibility of flame quenching in prechamber nozzles for small apertures due to heat loss that reduce the temperature of the burned gases in the turbulent jet and affect ignition in the main chamber. While the nozzle diameter is kept constant in the present work (d_{nozzle} = 3 mm), the wall temperature is another parameter that affects the heat loss. Additionally, non-adiabatic conditions occurring at (relatively) cold walls are found to hinder the consumption of N_2O formed during combustion because the consumption of N_2O is slowed down significantly at lower temperatures [36]. This is due to the limited activity of the N_2O consumption reactions and, as soon as combustion products are cooled down, these reactions only weakly contribute to N_2O reduction. Case 3 at stoichiometric conditions is taken as the reference conditions for the investigation of the effect of wall temperature: four wall temperatures T_{wall} = 500, 550, 600, 700 K are considered in Cases 5, 6, 7, and 3, respectively. Also for this parametric variation, the time history of the integrated total mass of NO_x and N_2O normalized by the overall lower

FIGURE 6 Contours of NH_3 mass fraction Y_{NH3} for Case 3 (ϕ = 1.0).

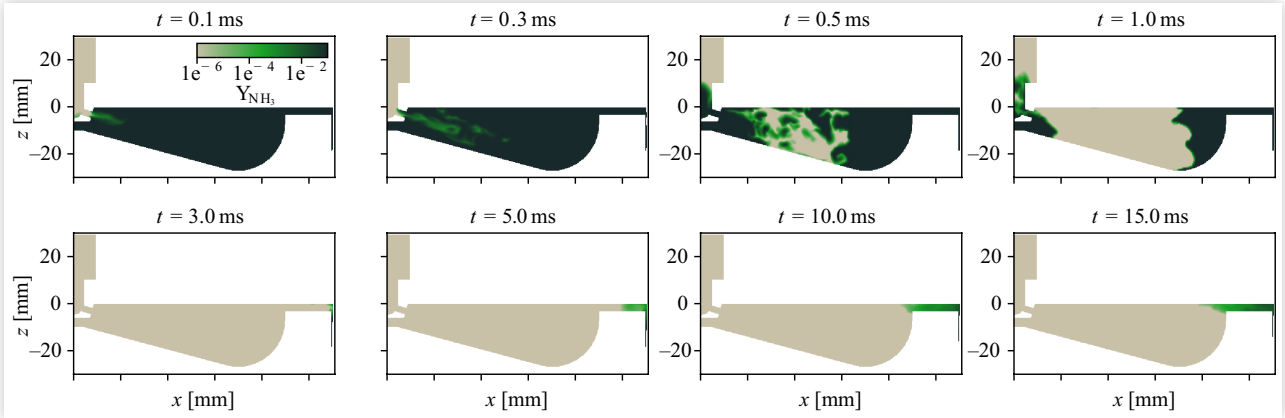

FIGURE 7 Contours of NO mass fraction Y_{NO}. Rows correspond to Case 2 (ϕ = 0.8, top) and Case 4 (ϕ = 1.2, bottom) and columns to different time instants.

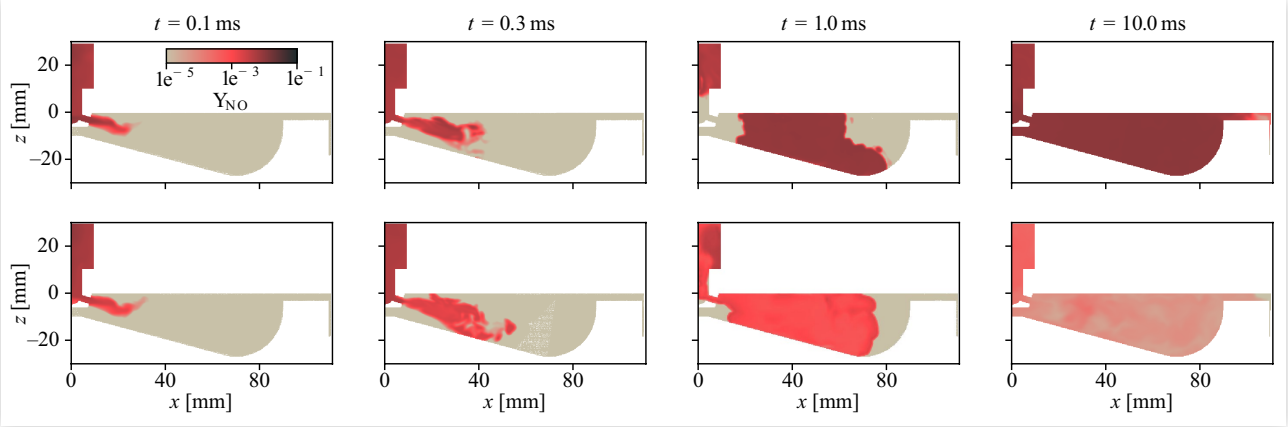

heating value of the hydrogen and ammonia fuel is shown in Figure 9. A significant effect of the wall temperature on the ignition of the main charge is observed. In Case 5, the lower wall temperature decreases the temperature of the turbulent jet, thereby effectively hindering ignition in the main chamber. At the higher wall temperatures considered in Cases 6–7 and 3, an obvious trend is evidenced linking increasing wall temperatures to faster ignition of the main charge. The formation of NO_x is clearly linked to the main charge combustion process, and NO_x consumption to the consumption of a part of the "leftover" H_2. Only small differences are observed in terms of the final normalized NO_x values at different wall temperatures but slightly lower values are observed for the higher wall temperatures. In terms of the N_2O emissions, the initial production is highest for the highest wall temperature, which is linked to the highest turbulent jet temperature. However, in all cases the total mass of N_2O drops sharply at the time of fastest NH_3 consumption before reaching a local minimum and slightly increasing again toward the final values. Interestingly, the final value seems to be closely related to the N_2O produced in the prechamber (as seen in Case 5 that did not ignite), and this initial N_2O is not consumed during the later stages of the combustion process. While differences in the final values are marginal, slightly larger N_2O emissions are observed for higher wall temperatures.

4.3. NH_3 Spray Injection and Non-premixed Combustion

In the previous section, the main chamber was initially filled with a homogeneous mixture of ammonia and air that is ignited by the hot turbulent hydrogen jet flames emerging from the prechamber. In the investigation described in the current section, the prechamber conditions and its geometry are unchanged. The main chamber, however, is now initially filled with air at 980 K. The ammonia main charge is then introduced into the main chamber through six liquid

FIGURE 8 Contours of N_2O mass fraction Y_{N2O} for Case 3 (ϕ = 1.0).

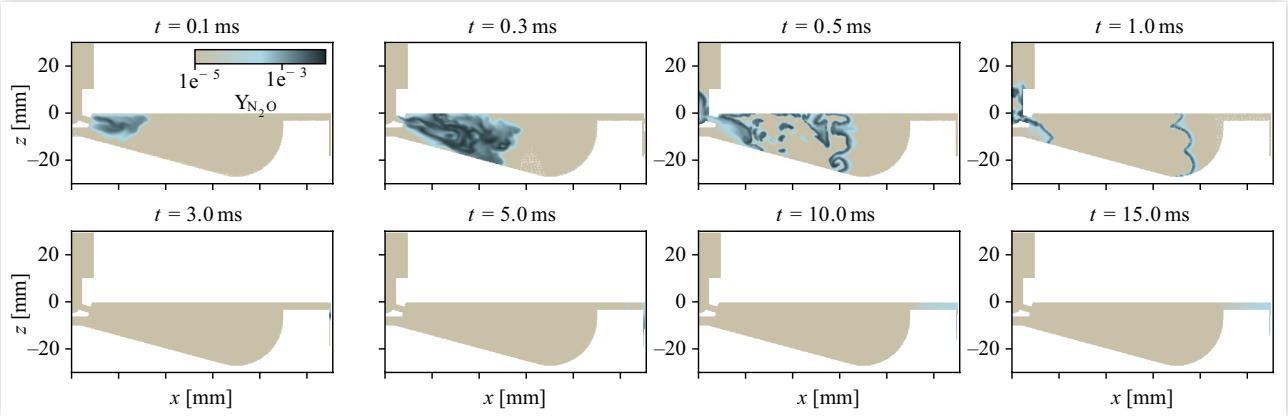

FIGURE 9 Time history of the integrated total mass of species NH_3, H_2 (a, b) and energy input-normalized NO_x and N_2O (c, d) for Cases 3 and 5–7.

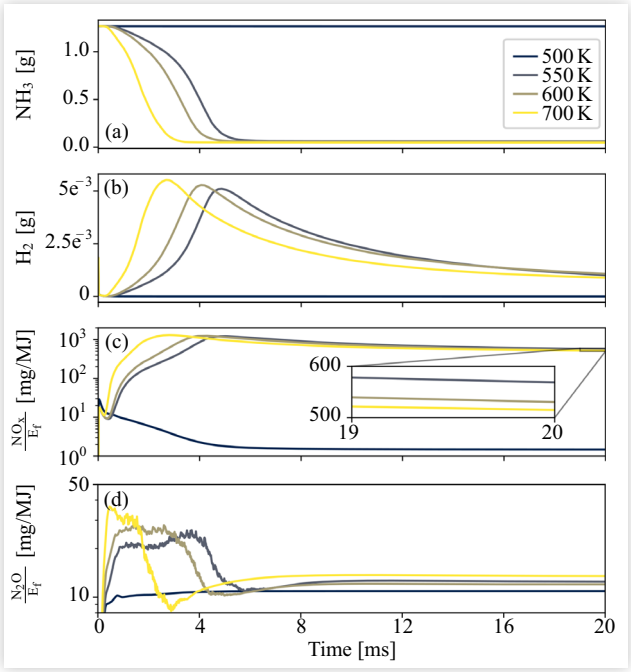

ammonia sprays. As described in Section 4.1, primary breakup and atomization of the liquid ammonia jet is not considered in the numerical model. Instead, a spray of liquid ammonia droplets with diameters of 12 µm is injected into the main chamber through the six nozzles, separated by a 60° angle and placed 15° and 45° from the neighboring prechamber nozzles providing the ignition source (refer to Figure 1 for a graphical representation of the relative position between ammonia sprays and hydrogen jet flames). The outer and inner cone angles of the ammonia sprays are set to 60° and 10°, respectively. The initial temperature and pressure in the main chamber are not sufficiently high to induce spontaneous ignition of the evaporating ammonia, as it is also the case for the premixed combustion configurations. This is the reason for the ignition source provided by the hydrogen-fired prechamber. Figure 10 shows the resulting local gas temperature and the mass fraction of the gaseous ammonia during injection before ignition of the prechamber. Two different times are shown: $t = 0.3$ (left) and 1.0 ms (right). By comparing the concentration of gaseous ammonia with the temperature, as shown in the upper row of Figure 10, it is clear that the evaporated ammonia results in a significant cooling of the gas phase. Actually, even though the initial temperature of the gas phase is 980 K, the evaporated ammonia may locally lead to temperatures of 300 K.

As a crucially important controlling parameter, the ignition of the hydrogen pilot charge in the prechamber can be initiated at any given time: before, during, and after the ammonia spray injection is taking place. In the following, the effect of different prechamber ignition times t_{ign} will be investigated. Here, t_{ign} is defined to be zero if the hydrogen in the prechamber is ignited at the same time as the ammonia spray is initiated. The ammonia spray injection has a duration of 1 ms, which means that t_{ign} = 1 ms corresponds to the prechamber ignition taking place at the same time as the last ammonia droplet is injected into the main combustion chamber.

Figure 11 provides a representation of the fuel injection, evaporation, ignition, and combustion process showing the time evolution of the gaseous ammonia mass fraction (light-dark green contours) in a cross-sectional plane located just underneath the fuel injection nozzles. The liquid ammonia droplets (gray spherical objects) are also visualized to illustrate the liquid spray shape and angle of injection relative to the turbulent hydrogen jet flames issuing from the prechamber into the combustion chamber. Regions where ammonia ignition has occurred—represented by high values of the OH-radical mass fraction (yellow-red contours)—are also shown. This visualization is based on results for Cases 8, 10, and 12. All cases that are depicted are initiated with the injection of the spray, but the prechamber is ignited at different t_{ign}. For the earliest ignition time (Case 8), the radical-rich combustion products of the prechamber get in contact with

FIGURE 10 Upper row shows contour of temperature for Case 12, while ammonia is shown in the lower row. The left column represents t = 0.3 ms, while t = 1 ms is shown for the right column. Gray dots represent ammonia droplets.

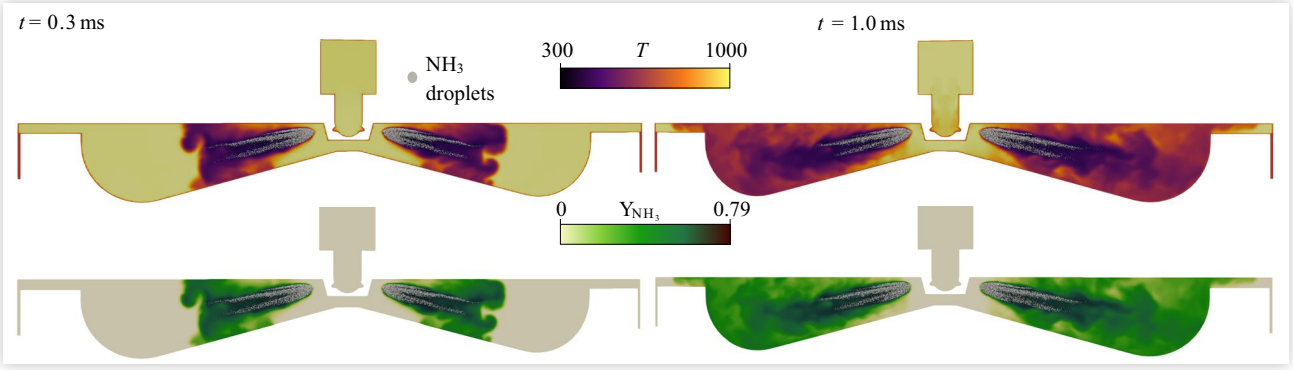

FIGURE 11 Representation of the injection, ignition, and combustion processes taking place within the main combustion chamber for Cases 8 (a)–(e), 10 (f)–(j), and 12 (k)–(n) for increasing time (rows). Gray spheres represent the ammonia droplets (only one of every hundred tracked droplets is shown). The instantaneous gas-phase ammonia and OH-radical mass fractions are shown in a cross-sectional plane located just underneath the fuel injection nozzles.

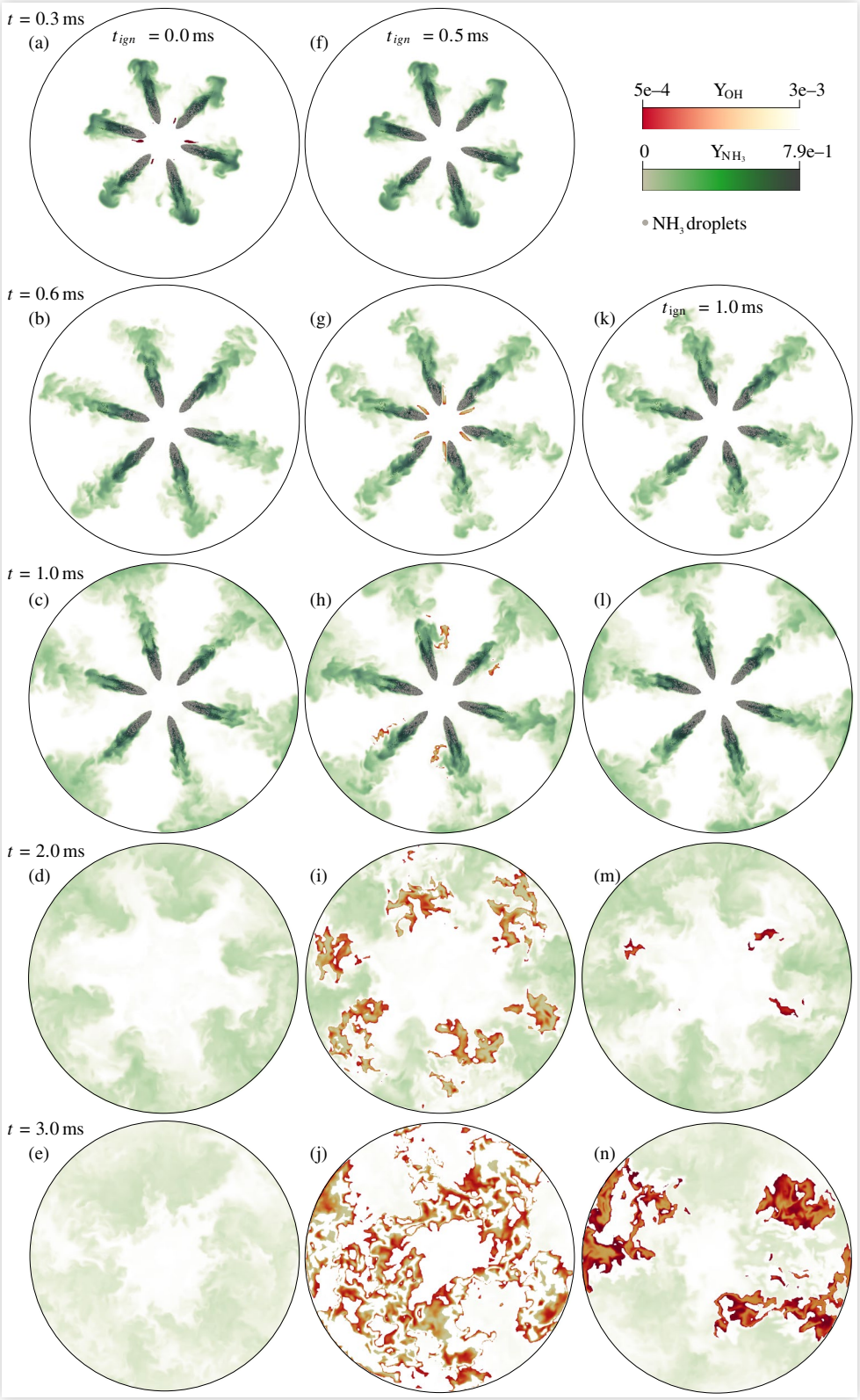

the partially evaporated ammonia spray at an early instant, when little mixing is achieved and fails to ignite the main charge. For Case 10, the ignition time is delayed by 0.5 ms. This allows for a better mixing and leads to a broader shear layer, with more favorable ignition conditions. In spite of the presence of high temperature and of a radical-rich gas-phase fluid mixture in proximity of the ammonia spray, the main charge does not immediately ignite. Ignition of the main charge occurs around $t = 1.0$ ms as illustrated in Figure 11(h). Subsequently, the combustion process progresses along the shear layer of the sprays where sufficient evaporation and mixing has already occurred, and then it eventually consumes the ammonia remaining in between the sprays. For the latest ignition time (Case 12), the ignition in the prechamber occurs at the instant when the spray injection is finished. This leads to strong mixing, specifically toward the outer walls, while little ammonia is present centrally in the chamber. The ignition of the main charge occurs late, around 1 ms after the ignition of the prechamber, which is slower than for Case 10. It is evident that the ignition was close to a misfire, as two of the prechamber jets are not able to ignite the adjacent ammonia sprays [top and bottom in Figure 11(m)]. However, the ignition is successful for the four other sprays. The slow ignition process gives the ammonia time to mix well, also toward the center and the flame continues to propagate along the outer walls, finally burning up the remaining unburnt gases in the center, when mixing has occurred there as well.

Figure 12 compares the temperature evolution in the non-premixed combustion configuration (solid lines) with the corresponding premixed combustion configuration (dashed line) at globally stoichiometric conditions. The temperature value corresponds to the averaged gas temperature across the whole computational domain volume. In the non-premixed combustion configuration, the initial injection and subsequent evaporation of the ammonia droplets cool down the main chamber. For the earliest prechamber ignition timing (Case 8), the hydrogen jet flames fail to ignite the ammonia main charge because the liquid droplets in the sprays have not had sufficient time to evaporate and mix with the oxidant air. For all later prechamber ignition timings, ignition of the main charge is successful. This is revealed by the rapid increase of the temperature value after the initial evaporation-induced drop. In contrast to the non-premixed combustion configuration, a noticeably higher peak temperature is reached in the premixed combustion configuration; however, the temperature value also decreases faster. The reason for the higher peak temperature is to be found in the fact that premixed combustion invariably takes place under stoichiometric conditions, minimizing the amount of hydrogen produced by ammonia dissociation in the flame. The subsequent decrease in temperature is due to the cooling effects of the walls. In the non-premixed combustion configuration, however, a significantly larger amount of hydrogen is produced by ammonia dissociation in the fuel-rich regions of the turbulent diffusion flames, leading to lower peak values of the mass-averaged temperature. The hydrogen so produced is then gradually consumed when turbulent mixing brings it in contact with available oxygen from the oxidant air. Similar trends are also observed for the other non-premixed combustion configurations with different ignition times. Here it is observed that, for the latest ignition time (Case 12), the longer mixing time available before ignition induces higher peak temperature and a steeper temperature decrease compared to the other cases with earlier ignition. The solid lines in Figure 13 illustrate the time history of the integrated total mass of the gaseous fuels and of the normalized emissions in the non-premixed (Cases 8–12, solid lines) and premixed configuration (Case 3, dashed line). Here, on the basis of a relevant engine rotational speed, we assume that the combustion process ends at $t = 20$ ms. This implies that the NO_x and N_2O emissions are defined as the amounts of these species present in the computational domain at $t = 20$ ms. Notably, as evidenced in Figure 13(b), the predicted amount of molecular hydrogen present at the end of the numerical simulations is significantly higher in the non-premixed configuration compared to the premixed one. The reason for this is that the hydrogen is produced from ammonia decomposition by the hot flame temperature at fuel-rich conditions and these conditions are not present in the premixed configuration. In the non-premixed configuration, however, due to the imperfect mixing of evaporated ammonia with air, a large variance of the mixture fraction occurs leading to a range of fuel-lean to fuel-rich conditions.

An important reason for investigating the non-premixed combustion configuration, and comparing it with the premixed one, is that the combustion process takes place primarily at fuel-rich conditions and it is expected to result in lower NO_x emissions. This is confirmed by inspection of Figure 13(c), illustrating that all non-premixed combustion simulations predict lower NO_x emissions. The other undesired species, N_2O, always abundant in the ammonia flame reaction layer, is typically consumed during the post-flame reaction process at idealized equilibrium conditions. However, as discussed in the previous section, this N_2O consumption

FIGURE 12 Time history of the averaged temperature in the non-premixed Cases 8–12 (solid lines) and in the homologous premixed Case 3 (dashed line) at stoichiometric conditions. The inset zooms in on the initial stages of the process (gray rectangle).

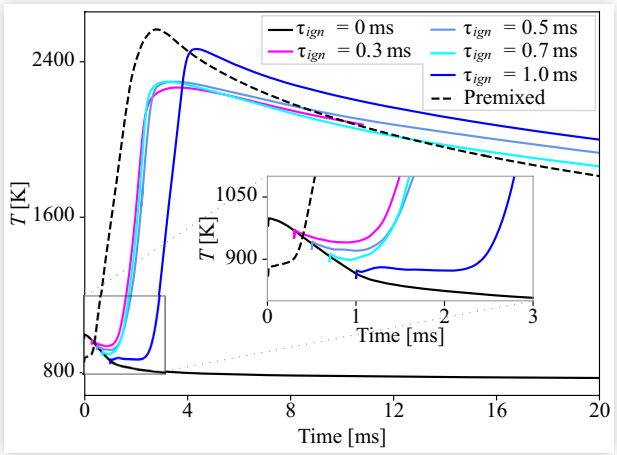

FIGURE 13 Time history of the integrated total mass of species NH_3, H_2 (a, b), and energy input-normalized NO_x and N_2O (c, d) for Cases 8–12 and Case 3.

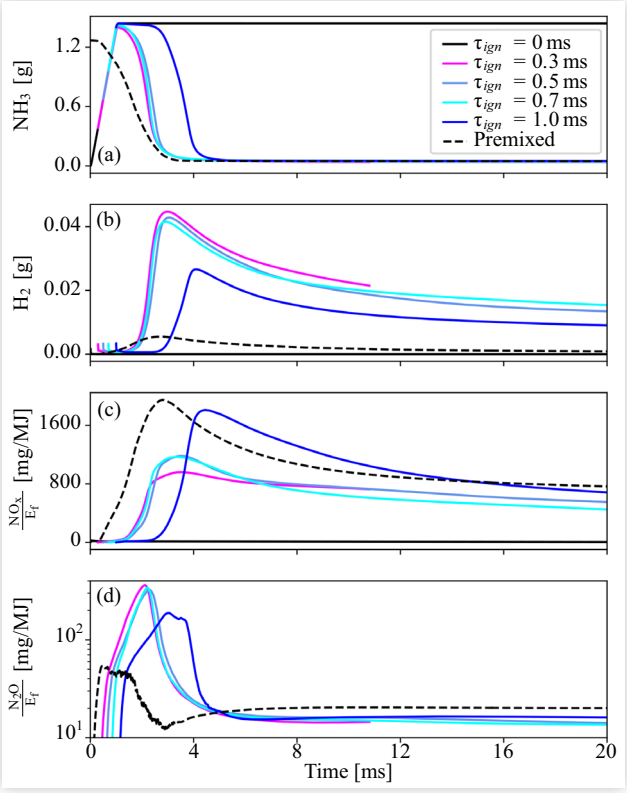

FIGURE 14 Time history of the integrated total mass of species NH_3, H_2 (a, b), and energy input-normalized NO_x and N_2O (c, d) in Cases 1, 10, and 13.

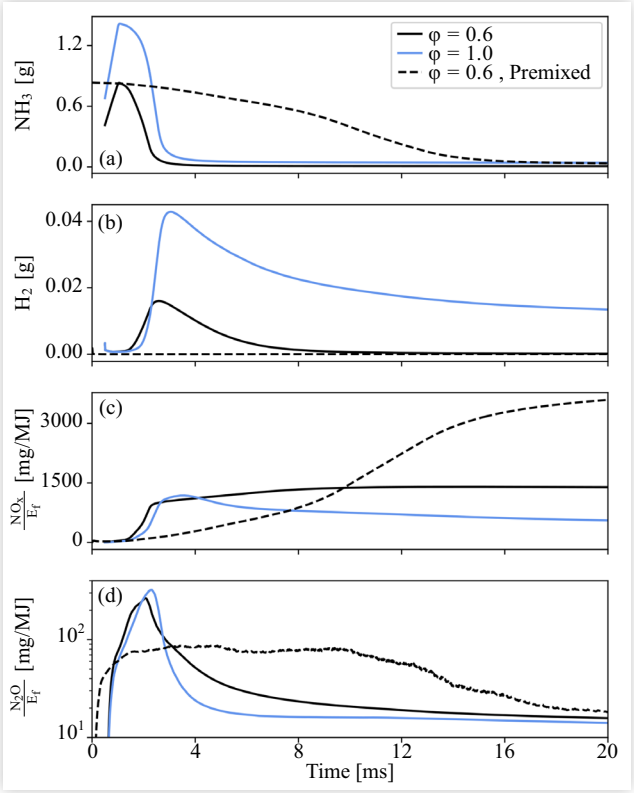

process is halted by strain-induced flame extinction or by non-adiabaticities due to flame–wall interaction and quenching with a (relatively) cold surface. In the premixed combustion configuration, a larger fraction of the combustion process takes place in close proximity to the wall once the premixed flame quenches onto it. Conversely, flame–wall interactions are greatly reduced in the non-premixed combustion configuration by its intrinsically different spatial pattern of fuel and oxidant distribution. Ultimately, this results in lower N_2O emissions for the non-premixed configuration as illustrated in Figure 13(d).

It can be observed from panels (b), (c), and (d) of Figure 13 that the non-premixed combustion configuration characterized by the latest ignition timing, having the longest fuel–oxidant mixing time prior to ignition, result in a time evolution of the combustion and emissions formation process that is most similar to the premixed combustion configuration. Earlier prechamber ignition timings result in combustion and emissions formation processes that are further away from the premixed results. Before concluding our comparative analysis of the non-premixed and premixed combustion configurations it is also important to investigate the predicted performance of a globally fuel-lean ammonia main charge. The time evolution of main fuel species and normalized emissions is shown in Figure 14. In the premixed combustion configuration at $\phi = 0.6$ (Case 1) ignition of the ammonia main charge by the prechamber hydrogen jet flames is not achieved and the ammonia is slowly consumed on a timescale not compatible with satisfactory combustion efficiency in a reciprocating piston engine. Conversely, in the homologous non-premixed combustion configuration at $\phi = 0.6$, the ammonia main charge is consumed even faster than at stoichiometric conditions. Due to the globally fuel-lean conditions, all hydrogen eventually produced during the ammonia combustion by its dissociation is rapidly oxidized by amply available oxygen and no unburnt hydrogen remains in the combustion chamber.

In terms of NO_x emissions, expected trends are observed with the premixed combustion configuration resulting in the largest normalized emissions followed by the globally fuel-lean non-premixed configuration. The globally stoichiometric non-premixed combustion configuration results in the lowest predicted NO_x emissions.

Finally, N_2O emissions are observed to reach similar levels for both the globally fuel-lean and stoichiometric non-premixed combustion configurations, as well as for the stoichiometric premixed combustion configuration, as shown in Figure 14(d).

In summary, direct injection into the combustion chamber of a liquid ammonia main charge, if combined with

a robust hydrogen-fired prechamber ignition source, seems to represent a viable design for clean and efficient ammonia-fired internal combustion engines. Such design strategy offers significant reductions in terms of emissions of undesired species and extends the engine operating range to leaner firing conditions. A minor disadvantage is the slight increase in the time needed to achieve complete fuel consumption at stoichiometric conditions. This could probably be circumvented by more sophisticated timing, e.g., by modifying conventional injection and ignition times to an earlier instant.

5. Conclusion

The present manuscript reports a numerical investigation of several premixed and non-premixed combustion configurations representative of ammonia-fired internal combustion engines operated in combination with a hydrogen-fired prechamber. An OpenFOAM-based LES framework is utilized to investigate the combustion behavior of the hydrogen-fired prechamber and the ammonia main charge. Two different injection strategies for the ammonia main charge are considered: a conventional port-injection configuration that assumes the presence of a homogeneous ammonia–air mixture in the combustion chamber and a direct-injection configuration in which liquid ammonia is introduced into the combustion chamber via six sprays. In the premixed combustion configuration, the equivalence ratio is shown to strongly affect the ignition and combustion behavior with the leanest case at $\phi = 0.6$, crucially, not achieving ignition and therefore resulting in an unusable operating condition for engine applications. For higher equivalence ratios, $\phi > 0.8$, ignition takes place and combustion is relatively fast, compatible with relevant engine rotational speeds, but remains incomplete, due to unburnt ammonia in the crevices. Strong equivalence ratio effects are also observed in terms of emissions of undesired species. Specifically, the richest case at $\phi = 1.2$ leads to a reduction in terms of the NO_x emission by two orders of magnitude compared to $\phi = 0.8$. Differences are also observed for N_2O, with fuel-rich operating conditions resulting in a reduction of N_2O emissions by almost an order of magnitude. The wall temperature also affects the rapidity of the ammonia main charge ignition but it is shown to only play a minor role in respect to emissions formation.

In the non-premixed combustion configuration, at certain conditions, robust ignition and significantly reduced emission levels of NO_x and N_2O are observed. For a global equivalence ratio of $\phi = 0.6$, in contrast to the equivalent premixed case, spray injection of the main charge leads to a successful rapid ignition and also reduces NO_x emission by a factor of four. While the emissions depend on the ignition timing, for $\phi = 1.0$, all spray cases lead to reduced emissions in terms of NO_x and N_2O compared to the premixed case. The ignition timing is able to gradually shift the non-premixed combustion configuration toward conditions that resemble the premixed combustion configuration in terms of fuel consumption and emissions. The results render the concept of combining a prechamber with spray injection of the main ammonia charge a promising strategy for ammonia-fired internal combustion engines. Careful optimization of the prechamber ignition timing relative to the initiation of the spray injection is shown to be crucially important to achieve ignition of the main charge.

Acknowledgements

The authors acknowledge support from the HYDROGENi Research Centre (333118) and the MaritimeNH3 (328679) project, with funding provided by the industry partners and by the Research Council of Norway.

Contact Information

Thomas Indlekofer, corresponding author
thomas.indlekofer@sintef.no

References

1. Law, L.C., Mastorakos, E., and Evans, S., "Estimates of the De-carbonization Potential of Alternative Fuels for Shipping as a Function of Vessel Type, Cargo, and Voyage," *Energies* 15, no. 20 (2022).
2. European Commission, "Fourth Annual Report from the European Commission on CO_2 Emissions from Maritime Transport," 2023.
3. "Casale History Timeline," accessed 12 August, 2024, https://casale.ch/about/.
4. Kroch, E., "Ammonia—A Fuel FOT Motor Buses," *J. Inst. Pet* 31 (1945): 213-223.
5. Cornelius, W., Huellmantel, L.W., and Mitchell, H.R., "Ammonia as an Engine Fuel," *SAE Transactions* 74 (1966): 300-326.
6. Imhoff, T.B., Gkantonas, S., and Mastorakos, E., "Analysing the Performance of Ammonia Powertrains in the Marine Environment," *Energies* 14, no. 21 (2021): 7447.
7. Erdemir, D. and Dincer, I., "A Perspective on the Use of Ammonia as a Clean Fuel: Challenges and Solutions," *International Journal of Energy Research* 45, no. 4 (2021): 4827-4834.
8. Valera-Medina, A., Amer-Hatem, F., Azad, A.K., Dedoussi, I.C. et al., "Review on Ammonia as a Potential Fuel: From Synthesis to Economics," *Energy & Fuels* 35 (2021): 6964-7029.
9. Bjørgen, K.O.P., Emberson, D.R., and Løvås, T., "Combustion of Liquid Ammonia and Diesel in a

Compression Ignition Engine Operated in High-Pressure Dual Fuel Mode," *Fuel* 360 (2024): 130269.

10. Scharl, V., Lackovic, T., and Sattelmayer, T., "Characterization of Ammonia Spray Combustion and Mixture Formation under High-Pressure, Direct Injection Conditions," *Fuel* 333 (2023): 126454.
11. Qi, Y., Liu, W., Liu, S., Wang, W. et al., "A Review on Ammonia-Hydrogen Fueled Internal Combustion Engines," *eTransportation* 18 (2023): 100288.
12. Comotti, M. and Frigo, S., "Hydrogen Generation System for Ammonia–Hydrogen Fuelled Internal Combustion Engines," *International Journal of Hydrogen Energy* 40, no. 33 (2015): 10673-10686.
13. Mørch, C., Bjerre, A., Gøttrup, M., Sorenson, S. et al., "Ammonia/Hydrogen Mixtures in an SI-Engine: Engine Performance and Analysis of a Proposed Fuel System," *Fuel* 90, no. 2 (2011): 854-864.
14. Frigo, S. and Gentili, R., "Analysis of the Behaviour of a 4-Stroke SI Engine Fuelled with Ammonia and Hydrogen," *International Journal of Hydrogen Energy* 38, no. 3 (2013): 1607-1615; in *2011 Zing International Hydrogen and Fuel Cells Conference: From Nanomaterials to Demonstrators*.
15. Alvarez, C.E.C., Couto, G.E., Roso, V.R., Thiriet, A.B. et al., "A Review of Prechamber Ignition Systems as Lean Combustion Technology for SI Engines," *Applied Thermal Engineering* 128 (2018): 107-120.
16. Malé, Q., Staffelbach, G., Vermorel, O., Misdariis, A. et al., "Large Eddy Simulation of Pre-chamber Ignition in an Internal Combustion Engine," *Flow, Turbulence and Combustion* 103 (2019): 465-483.
17. Boretti, A.A., "Novel Heavy Duty Engine Concept for Operation Dual Fuel H_2–NH_3," *International Journal of Hydrogen Energy* 37, no. 9 (2012): 7869-7876; in *7th Petite Workshop on the Defect Chemical Nature of Energy Materials*, Storaas, Kongsberg, Norway, March 14–17, 2011.
18. Liu, Z., Zhou, L., Zhong, L., Liu, P. et al., "Experimental Investigation on the Combustion Characteristics of NH_3/H_2/Air by the Spark Ignition and Turbulent Jet Ignition," *Combustion Science and Technology* 196 (2022): 73-94.
19. Liu, Z., Zhou, L., Zhong, L., and Wei, H., "Enhanced Combustion of Ammonia Engine Based on Novel Air-Assisted Pre-chamber Turbulent Jet Ignition," *Energy Conversion and Management* 276 (2023): 116526.
20. Zhang, X., Tian, J., Cui, Z., Xiong, S. et al., "Visualization Study on the Effects of Pre-chamber Jet Ignition and Methane Addition on the Combustion Characteristics of Ammonia/Air Mixtures," *Fuel* 338 (2023): 127204.
21. Zhou, L., Zhong, L., Liu, Z., and Wei, H., "Toward Highly-Efficient Combustion of Ammonia–Hydrogen Engine: Prechamber Turbulent Jet Ignition," *Fuel* 352 (2023): 129009.
22. Kobayashi, H., Hayakawa, A., Somarathne, K., and Okafor, E., "Science and Technology of Ammonia Combustion," *Proceedings of the Combustion Institute* 37, no. 1 (2019): 109-133.
23. Valera-Medina, A., Gutesa, M., Xiao, H., Pugh, D. et al., "Premixed Ammonia/Hydrogen Swirl Combustion under Rich Fuel Conditions for Gas Turbines Operation," *International Journal of Hydrogen Energy* 44 (2019): 8615-8626.
24. Elbaz, A.M., Wang, S., Guiberti, T.F., and Roberts, W.L., "Review on the Recent Advances on Ammonia Combustion from the Fundamentals to the Applications," *Fuel Communications* 10 (2022): 100053.
25. Hayakawa, A., Hayashi, M., Kovaleva, M., Gotama, G.J. et al., "Experimental and Numerical Study of Product Gas and N_2O Emission Characteristics of Ammonia/Hydrogen/Air Premixed Laminar Flames Stabilized in a Stagnation Flow," *Proceedings of the Combustion Institute* 39, no. 2 (2023): 1625-1633.
26. Yang, W., Ranga Dinesh, K., Luo, K., and Thevenin, D., "Direct Numerical Simulation of Turbulent Premixed Ammonia and Ammonia Hydrogen Combustion under Engine-Relevant Conditions," *International Journal of Hydrogen Energy* 47 (2022): 11083-11100.
27. Pham, V.C., Kim, J.K., Lee, W.-J., Choe, S.-J. et al., "Effects of Piston Bowl Geometry on Combustion and Emissions of a Four-Stroke Heavy-Duty Diesel Marine Engine," *Applied Sciences* 12, no. 24 (2022): 13012.
28. Weller, H.G., Tabor, G., Jasak, H., and Fureby, C., "A Tensorial Approach to Computational Continuum Mechanics Using Object-Oriented Techniques," *Computers in Physics* 12 (1998): 620-631.
29. Jiang, Y., Gruber, A., Seshadri, K., and Williams, F., "An Updated Short Chemical-Kinetic Nitrogen Mechanism for Carbon-Free Combustion Applications," *International Journal of Energy Research* 44, no. 2 (2020): 795-810.
30. Scharl, V. and Sattelmayer, T., "Ignition and Combustion Characteristics of Diesel Piloted Ammonia Injections," *Fuel Communications* 11 (2022): 100068.
31. Li, T., Zhou, X., Wang, N., Wang, X. et al., "A Comparison between Low- and High-Pressure Injection Dual-Fuel Modes of Diesel-Pilot-Ignition Ammonia Combustion Engines," *Journal of the Energy Institute* 102 (2022): 362-373.
32. Pei, Y., Hawkes, E.R., and Kook, S., "A Comprehensive Study of Effects of Mixing and Chemical Kinetic Models on Predictions of n-Heptane Jet Ignitions with the PDF Method," *Flow, Turbulence and Combustion* 91 (2013): 249-280.
33. Haugsvar, M., "Computational Fluid Dynamic Simulations of liquid Ammonia Spray," Master's thesis, NTNU, 2023.

34. Duynslaegher, C., Jeanmart, H., and Vandooren, J., "Flame Structure Studies of Premixed Ammonia/Hydrogen/Oxygen/Argon Flames: Experimental and Numerical Investigation," *Proceedings of the Combustion Institute* 32, no. 1 (2009): 1277-1284.

35. Zhou, L., Song, Y., Hua, J., Liu, F. et al., "Effects of Different Hole Structures of Pre-chamber with Turbulent Jet Ignition on the Flame Propagation and Lean Combustion Performance of a Single-Cylinder Engine," *Fuel* 308 (2022): 121902.

36. Pedersen, K.A., Lewandowski, M.T., Schulze-Netzer, C., Pasternak, M. et al., "Ammonia in Dual-Fueled Internal Combustion Engines: Impact on NOx, N_2O, and Soot Formation," *Energy & Fuels* 37 (2023): 17585-17604.